





Article

Unveiling the Potential of B₃O₃ Nanoflake as Effective Transporter for the Antiviral Drug Favipiravir: Density Functional Theory Analysis

Muhammad Nauman Zahid ^{1,†} , Naveen Kosar ^{2,†}, Hasnain Sajid ³, Khalid Elfaki Ibrahim ⁴ ,
Mansour K. Gatasheh ⁵  and Tariq Mahmood ^{6,7,*} 

¹ Department of Biology, College of Science, University of Bahrain, Sakhir P.O. Box 32038, Bahrain; nzahid@uob.edu.bh

² Department of Chemistry, University of Management and Technology (UMT), C-11, Johar Town Lahore, Lahore 54770, Pakistan; naveenflavia@gmail.com

³ School of Science and Technology, Nottingham Trent University, Clifton Lane, Nottingham NG11 8NS, UK; hasnainmsajid@yahoo.com

⁴ Department of Zoology, College of Science, King Saud University, P.O. Box 2455, Riyadh 11451, Saudi Arabia; kibrahim@ksu.edu.sa

⁵ Department of Biochemistry, College of Science, King Saud University, P.O. Box 2455, Riyadh 11451, Saudi Arabia; mgatasheh@ksu.edu.sa

⁶ Department of Chemistry, COMSATS University, Abbottabad Campus, Abbottabad 22060, Pakistan

⁷ Department of Chemistry, College of Science, University of Bahrain, Sakhir P.O. Box 32038, Bahrain

* Correspondence: tmahmood@uob.edu.bh

† These authors contributed equally to this work.

Abstract: In this study, for the first time, boron oxide nanoflake is analyzed as drug carrier for favipiravir using computational studies. The thermodynamic stability of the boron oxide and favipiravir justifies the strong interaction between both species. Four orientations are investigated for the interaction between the favipiravir and the B₃O₃ nanoflake. The E_{int} of the most stable orientation is −26.98 kcal/mol, whereas the counterpoise-corrected energy is −22.59 kcal/mol. Noncovalent interaction index (NCI) and quantum theory of atoms in molecules (QTAIM) analyses are performed to obtain insights about the behavior and the types of interactions that occur between B₃O₃ nanoflake and favipiravir. The results indicate the presence of hydrogen bonding between the hydrogen in the favipiravir and the oxygen in the B₃O₃ nanoflake in the most stable complex (FAV@B₃O₃-C1). The electronic properties are investigated through frontier molecular orbital analysis, dipole moments and chemical reactivity descriptors. These parameters showed the significant activity of B₃O₃ for favipiravir. NBO charge analysis transfer illustrated the charge transfer between the two species, and UV-VIS analysis confirmed the electronic excitation. Our work suggested a suitable drug carrier system for the antiviral drug favipiravir, which can be considered by the experimentalist for better drug delivery systems.

Keywords: B₃O₃; Favipiravir; DFT; Drug delivery; QTAIM



Citation: Zahid, M.N.; Kosar, N.; Sajid, H.; Ibrahim, K.E.; Gatasheh, M.K.; Mahmood, T. Unveiling the Potential of B₃O₃ Nanoflake as Effective Transporter for the Antiviral Drug Favipiravir: Density Functional Theory Analysis. *Molecules* **2023**, *28*, 8092. <https://doi.org/10.3390/molecules28248092>

Academic Editor: Chan Kyung Kim

Received: 10 November 2023

Revised: 23 November 2023

Accepted: 28 November 2023

Published: 14 December 2023



Copyright: © 2023 by the authors. Licensee MDPI, Basel, Switzerland. This article is an open access article distributed under the terms and conditions of the Creative Commons Attribution (CC BY) license (<https://creativecommons.org/licenses/by/4.0/>).

1. Introduction

Favipiravir (FAV) is an antiviral drug that has shown potential in the treatment of several RNA viruses, including influenza, Ebola virus, and, most recently, SARS-CoV-2, the virus responsible for the COVID-19 pandemic [1]. Favipiravir, also known as T-705, was initially developed as an influenza drug and works by selectively inhibiting the RNA-dependent RNA polymerase (RdRp) of the virus, thereby preventing viral replication [2]. The chemical name of favipiravir is 6-fluoro-3-hydroxy-2-pyrazine carboxamide, and its molecular formula is C₅H₄FN₃O. The structure of favipiravir consists of a pyrazine ring linked to a carboxamide group, with a fluorine atom and a hydroxyl group attached at positions 6 and 3 [3].

In a study conducted by Furuta et al. (2013), favipiravir demonstrated potent antiviral activity against the influenza virus *in vitro* and in animal models [2]. Additionally, in a clinical trial conducted in Japan during the 2014 Ebola outbreak, favipiravir showed efficacy in reducing mortality rates [4]. More recently, several studies have evaluated the efficacy of favipiravir as a treatment for COVID-19. In a randomized clinical trial conducted in China, patients treated with favipiravir had a shorter time for fever resolution and improved radiological findings compared to the control group [5]. In another study conducted in India, favipiravir was found to significantly improve clinical recovery in COVID-19 patients compared to standard care [6]. Overall, favipiravir has shown promise as a potential treatment for several RNA viruses, including SARS-CoV-2.

Drug delivery systems (DDS) refer to the technologies used to deliver therapeutic agents to their intended targets in the body. The development of DDS has revolutionized the field of medicine by enabling targeted and controlled drug release, improving therapeutic efficacy, and minimizing side effects [7,8]. One promising area of research in DDS is the use of nanomaterials for drug delivery, which offers advantages such as high drug loading capacity, prolonged circulation time, and enhanced bioavailability [9,10].

Various nanostructures, including nanosheets, nanocages, and nanoparticles, have been successfully employed for drug delivery systems, as reported in the literature [11–18]. Among these, carbon-based nanomaterials have become increasingly popular due to their high efficiency [19–22]. For instance, graphdiyne has been used to effectively deliver sorafenib and regorafenib [23]. While graphene sheets have also been reported for drug delivery systems [24,25], their limited chemical mobility restricts their use for many drugs [26,27]. Recent studies indicate that boron oxide nanosheets (B_3O_3) offer several advantages over graphene nanosheets. B_3O_3 has a reactive hollow cavity in comparison to graphene, which makes it a more attractive option [28].

Boron oxide nanosheets (B_3O_3) are a type of two-dimensional nanomaterial with a hexagonal lattice structure. B_3O_3 nanosheets have been investigated for various applications, including catalysis, electronic devices, and biomedical applications such as drug delivery [29–32]. Experimental and theoretical studies have confirmed that B_3O_3 nanosheets possess a hexagonal planar structure, with strong covalent bonds between the boron atoms. The six-fold symmetry of this structure has been reported in both experimental [33] and theoretical studies [34]. The formation of B_3O_3 nanosheets occurs through the condensation of three tetrahydroxydiboron molecules [35], which connect six B_3O_3 hexagons to create a porous structure with a surface area of 2.32 Å. This porous structure is ideal for attracting analytes. In 2018, Lin et al. theoretically designed a porous B_3O_3 nanosheet [36] with a flat surface with identical pores, as reported in the literature. B_3O_3 nanosheets have shown promise as a DDS due to their biocompatibility, low toxicity, and ability to encapsulate drugs and release them in a controlled manner [35,37,38].

B_3O_3 nanosheets have shown promise for delivering anticancer agents. For example, the nanosheets were functionalized with a targeting agent and demonstrated enhanced accumulation in cancer cells, leading to increased therapeutic efficacy [39]. B_3O_3 monolayers have been investigated as potential carriers for a flutamide-based anticancer drug delivery system [36]. Similarly, magnetic boron nitride nanosheets have been utilized as pH-responsive smart nanocarriers for the delivery of doxorubicin in the treatment of liver cancer [40].

Our study will employ density functional theory (DFT) calculations, powerful tools for rationalizing experimentally observed phenomena and predicting the behavior, properties, and applications of various systems [41,42]. Despite their potential, there are no reports in the literature exploring the use of B_3O_3 nanoflake as antiviral drug carrier for favipiravir. Therefore, we aim to propose B_3O_3 as a drug carrier for this antiviral drug. We hypothesize that B_3O_3 has the potential to serve as a drug carrier for favipiravir. Our results support our hypothesis, as we observed excellent interaction energies between favipiravir and B_3O_3 nanoflakes.

2. Results

2.1. Geometric and Energetic Analysis

For exploring the interaction of favipiravir with B_3O_3 nanoflake, four different orientations are chosen. These orientations are as follows: (i) favipiravir is adsorbed horizontally on the B_3O_3 surface (FAV@ B_3O_3 -C); (ii) the amino group is directed toward the center of the B_3O_3 surface (FAV@ B_3O_3 -C1); (iii) the aromatic ring containing fluoride is directed towards the center of the B_3O_3 surface (FAV@ B_3O_3 -C3); and (iv) favipiravir is adsorbed on the side of the B_3O_3 surface (FAV@ B_3O_3 -SW1). The optimized energy minima structures of the individual drug, B_3O_3 nanoflakes and all complexes are given in Figures 1 and 2. The prominent interacting distances (d_{int}), interaction energies (E_{int}) and counterpoise-counterpoise energies (E_{cp}) are summarized in Table 1. Geometric optimization is followed by vibrational analysis, which confirmed that these optimized structures represent the true minima on the potential energy surface. The optimized configurations revealed the highly reactive nature of the porous cavity of B_3O_3 and its strong propensity for binding with incoming molecules. The respective observed counterpoise-corrected energies (E_{cp}) for the optimized complexes were -20.08 , -22.59 , -20.70 and -10.66 kcal/mol for the orientations FAV@ B_3O_3 -C, FAV@ B_3O_3 -C1, FAV@ B_3O_3 -C3 and FAV@ B_3O_3 -SW1, respectively. The E_{cp} values are comparable to interaction energies (E_{int})—see Table 1. The reason for the stability (as shown by exothermic reactions) of these complexes is the presence of various strong noncovalent interactions between the drug and the surface.

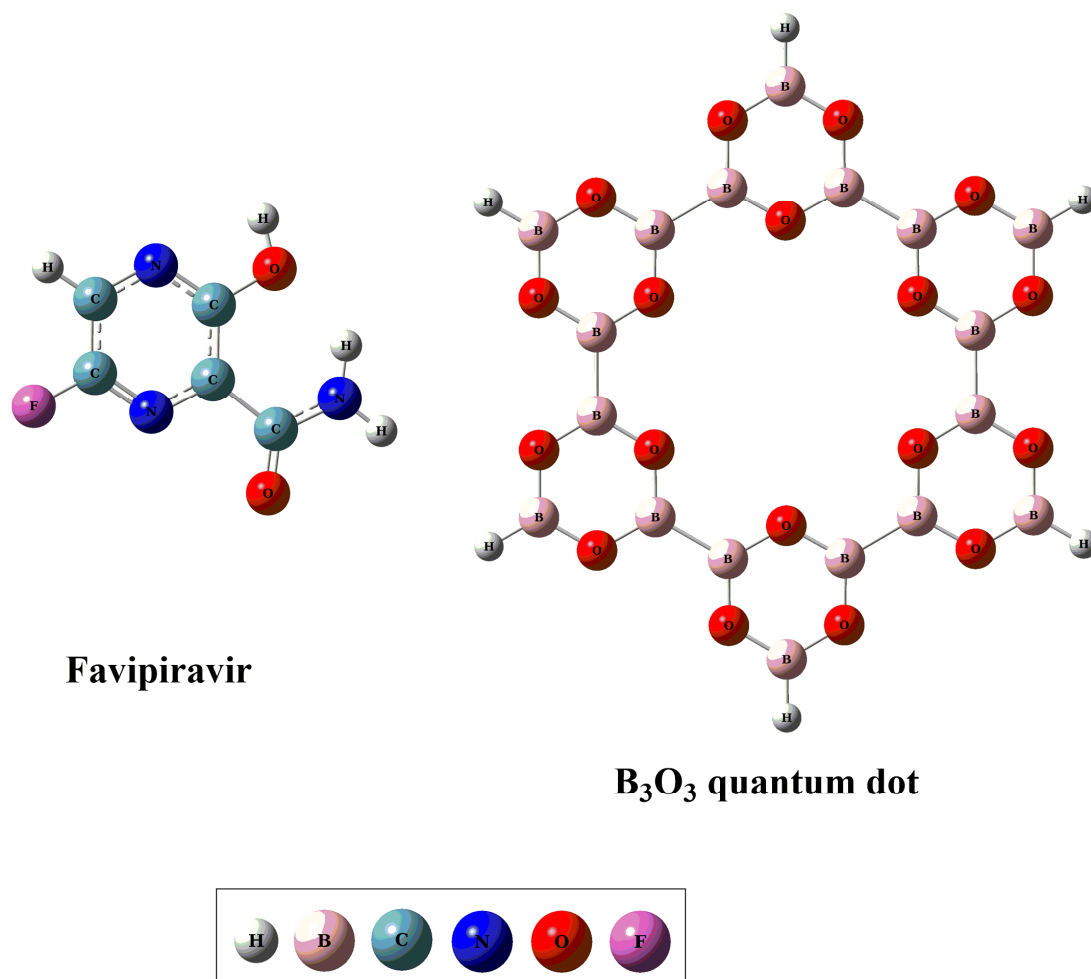


Figure 1. The optimized geometries of bare favipiravir and the B_3O_3 nanoflake.

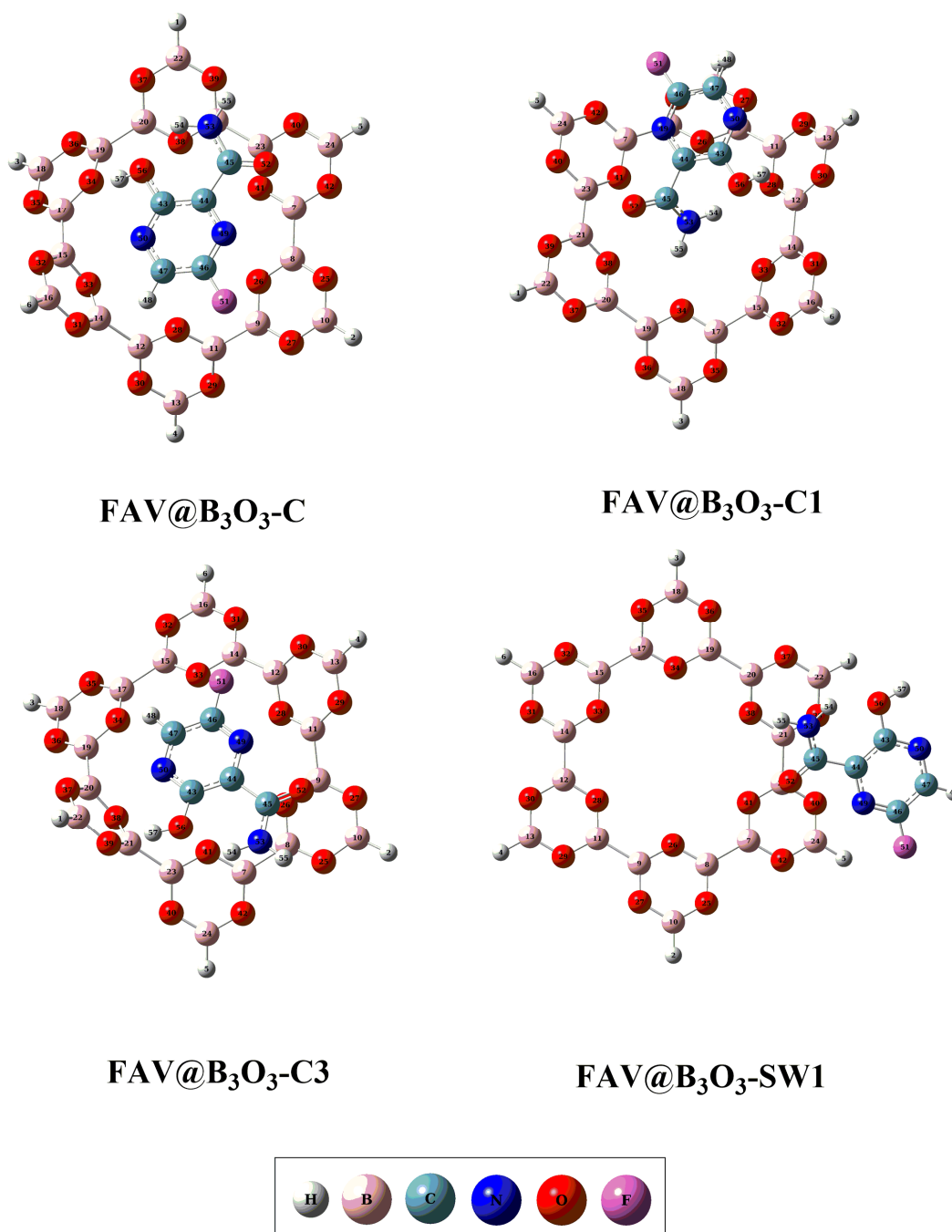


Figure 2. The optimized geometries of FAV@B₃O₃ nanoflake complexes such as FAV@B₃O₃-C, FAV@B₃O₃-C1, FAV@B₃O₃-C3 and FAV@B₃O₃-SW1.

The larger E_{cp} value ($-22.59 \text{ kcal mol}^{-1}$) for FAV@B₃O₃-C1 indicates that the NH₂ group of the drug possesses more electropositive protons, which can form strong interactions with the oxygen atoms of B₃O₃, resulting in higher interaction energy. The reason for these strong interactions is the presence of oxygen, which has great affinity for the electropositive hydrogen atoms of the amine group. Consequently, these highly electropositive hydrogen atoms exhibit stronger interactions with the electron-rich cavities of the B₃O₃ surface through hydrogen bonding. FAV@B₃O₃-C1 has two hydrogen bonds, leading to a higher E_{cp} compared to FAV@B₃O₃-C, which has only one hydrogen bond between the hydrogen of the hydroxyl group of favipiravir and the oxygen of the B₃O₃ surface. However, in FAV@B₃O₃-C3, an additional interaction occurs between the fluoride of favipiravir and the boron atoms of the B₃O₃ surface. The additional halogen interaction between

fluoride and the surface gives more stability to FAV@B₃O₃-C3 compared to FAV@B₃O₃-C. Due to the fewer interactions and lower electronegativity on the sides of B₃O₃, the E_{cp} value for FAV@B₃O₃-SW1 is significantly lower than that of the other three complexes (FAV@B₃O₃-C, FAV@B₃O₃-C1 and FAV@B₃O₃-C3). These findings also demonstrate that E_{cp} increases as the interacting distances (d_{int}) decrease. The important interaction distances are given in Table 1, and the interacting distance (d_{int}) of the first bond is up to 2 Å for all complexes except for the FAV@B₃O₃-SW1 complex. The d_{int} of the second bond is lower for FAV@B₃O₃-C1 (2.27 Å), followed by FAV@B₃O₃-C3 (2.57 Å) and FAV@B₃O₃-C (2.70 Å). The largest d_{int} is seen for FAV@B₃O₃-SW1 (3.01 Å). These results align with the existing literature indicating an inverse relationship between thermodynamic stability and distance [43,44].

Table 1. Interaction energies (E_{int}), interacting atoms (A_{int}), interacting distances (d_{int}), and counterpoise-corrected energies (E_{cp}) of reported FAV@B₃O₃ complexes.

Complexes	E _{int} (kcal/mol)	A _{int}	d _{int} (Å)	E _{cp} (kcal/mol)
FAV@B ₃ O ₃ -C	−23.84	H57—O34	1.84	−20.08
		H48—O28	2.70	
FAV@B ₃ O ₃ -C1	−26.98	H55—O34	2.13	−22.59
		H54—O28	2.27	
FAV@B ₃ O ₃ -C3	−24.47	H57—O39	1.94	−20.70
		H48—O34	2.57	
FAV@B ₃ O ₃ -SW1	−12.55	O52—B23	2.71	−10.66
		N49—O40	3.01	

2.2. Noncovalent Interactions (NCI) Analysis

The noncovalent interactions between the surface and analyte (drug) for the deeper visualization are evaluated through NCI analysis. The results of the NCI plots are presented in two forms; 2D RDG scattered graphs and 3D isosurfaces. The 2D RDG scattered graphs and 3D isosurfaces for our designed complexes are given in Figure 3. In this analysis, the nature of the interactions is represented by three colors, namely red, blue and green. The blue, green and red colors represent strong hydrogen bonding interactions, London dispersion interactions and steric repulsion between the analyte and surface, respectively [38,45–47].

The scattered graphs of RDG are generated on the basis of the mathematical equation given below.

$$\text{RDG} = \frac{1}{2(3\pi^2)^{1/3}} \frac{|\nabla\rho|}{\rho^{4/3}}$$

where $\nabla\rho$ represents the average reduced density gradient. The λ_2 term in the sign $\lambda_2(\rho)$ function is obtained using the RDG method as the second largest eigenvalue of the average electron density Hessian matrix computed throughout the dynamical trajectory. It provides information about the different types of weak interactions in a system. The existence of green spikes between -0.020 and 0.001 au in the 2D RDG map evidences the presence of dominant dispersion forces (van der Waals forces) in all complexes. There are some blue spikes in the 2D RDG map depicting hydrogen bonding between the hydrogen of the amino group (in Favipiravir) and the oxygen of B₃O₃ in all complexes. The red spikes in the RDG scatter maps show intermolecular steric repulsion in all complexes. These results indicate a stronger influence of van der Waal's interactions and hydrogen bonding.

Furthermore, the 3D isosurfaces are plotted at an isosurface value of 0.05 au. The strength of nonbonding interactions between the analyte and the surface is estimated based on the thickness of the patches. The stippled patches show weak interactions,

but thick patches indicate strong interactions between the analyte (Favipiravir) and the surface (B_3O_3).

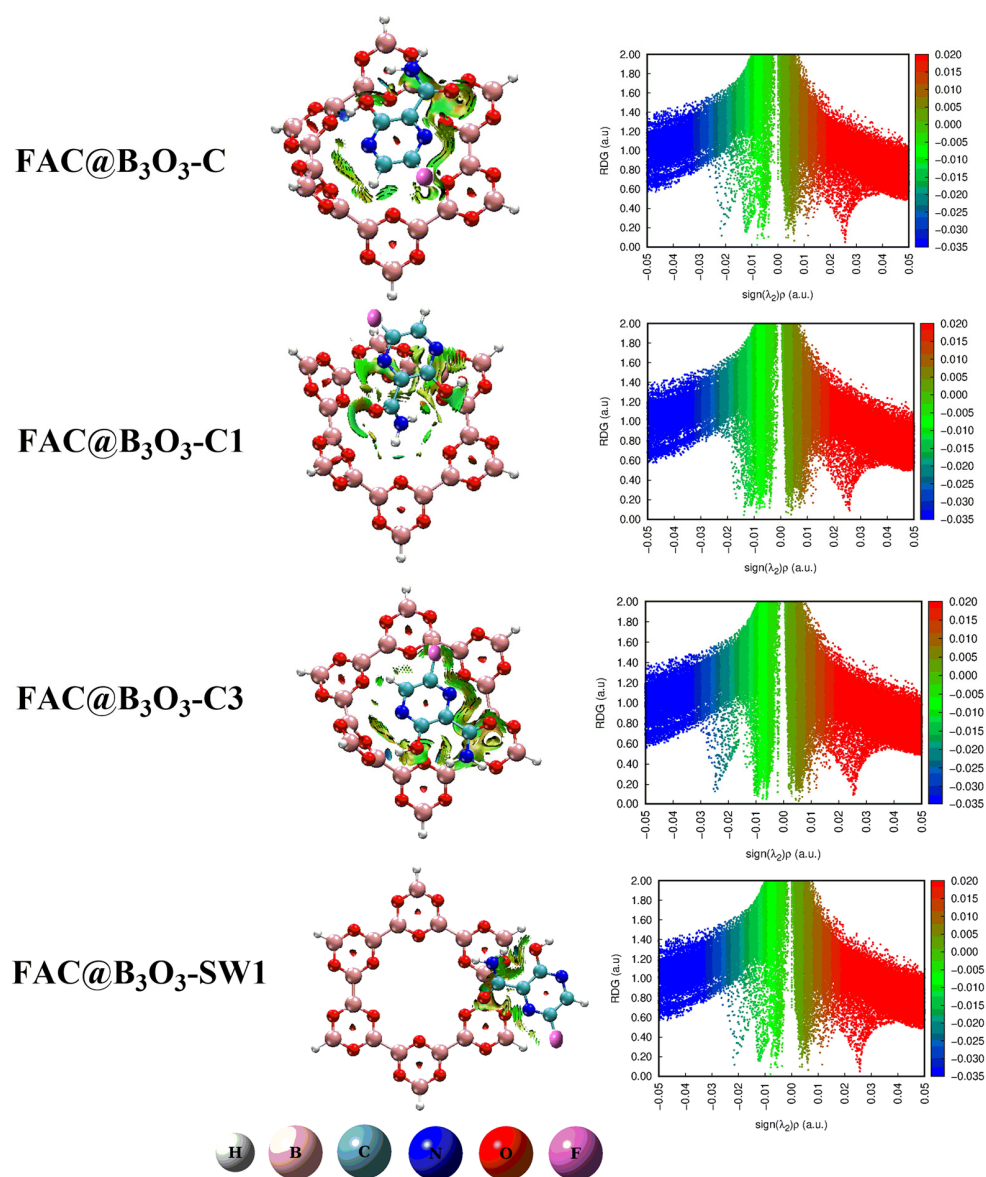


Figure 3. Two-dimensional RDG scattered graphs (right) and 3D isosurfaces (left) of favipiravir@ B_3O_3 complexes (FAV@ B_3O_3 -C, FAV@ B_3O_3 -C1, FAV@ B_3O_3 -C3, FAV@ B_3O_3 -SW1).

All complexes (FAV@ B_3O_3 -C, FAV@ B_3O_3 -C1, FAV@ B_3O_3 -C3, FAV@ B_3O_3 -SW1) show dark green thick patches which depict strong dispersion interactions between favipiravir and B_3O_3 . However, the thickness of these patches is less in the FAV@ B_3O_3 -C and FAV@ B_3O_3 -SW1 complexes as compared to the FAV@ B_3O_3 -C1 and FAV@ B_3O_3 -C3 complexes. We also noticed small red patches which illustrate steric repulsion between favipiravir and B_3O_3 . The blue patches indicate the hydrogen bonding between the hydrogen of the amino groups (in favipiravir) and the oxygen of B_3O_3 . The most pronounced blue patches are seen in the FAV@ B_3O_3 -C1 complex. The outcomes of both the 2D RDG graphs and the 3D isosurfaces illustrate the stability of these complexes. The results of NCI are consistent with the interaction energy results (vide supra).

2.3. Quantum Theory of Atoms in Molecules (QTAIM) Analysis

QTAIM analysis is a topological technique used to estimate the nature and strength of interactions between chemical species such as adsorbent (Favipiravir) and surface (B_3O_3). The electronic density (ρ), Laplacian electron density ($\nabla^2\rho$), and the sum of electron densities (H) are important parameters in QTAIM results to differentiate between the covalent and noncovalent interactions. The sum of electron densities (H) at bond critical points (BCPs) is the sum of kinetic and potential energy densities [48,49], which can be calculated using the equation below.

$$H = G + V$$

In the above equation, G and V represent the kinetic and potential energy densities. The H value is either zero or less than zero for all types of noncovalent interaction. Meanwhile, an H value greater than zero indicates significant electronic contribution and represents the covalent nature of the interaction. For close shell interactions, the kinetic energy density dominant over potential energy density where H is positive. The total electronic density produces the total electronic energy when integrated over all of the space [48]. A value of electron density (ρ) less than 0.1 au indicates the presence of non-covalent interactions with a positive value of Laplacian electron density ($\nabla^2\rho$) and sum of electron densities (H).

To examine the interactions more deeply and find bond critical points (BCPs) of favipiravir-adsorbed B_3O_3 complexes (FAV@ B_3O_3 -C, FAV@ B_3O_3 -C1, FAV@ B_3O_3 -C3, FAV@ B_3O_3 -SW1), the QTAIM analysis is performed, and the results are given in Table 2 and the BCPs are shown in Figure 4.

Table 2. QTAIM parameters including the electronic density (ρ), Laplacian electron density ($\nabla^2\rho$), kinetic energy density (G), potential energy density (V) and the sum of electron densities (H) at bond critical points (BCPs) in favipiravir-adsorbed B_3O_3 complexes (B_3O_3 -1-FAV-C, B_3O_3 -1-FAV-C-1, B_3O_3 -1-FAV-C-3, and B_3O_3 -1-FAV-C-SW1 in au).

BCPs	Ana-Surface	ρ	$\nabla^2\rho$	G	V	H
FAV@ B_3O_3 -C						
78	N49-O26	0.60×10^{-2}	0.21×10^{-1}	0.44×10^{-2}	-0.36×10^{-2}	0.79×10^{-3}
130	H57-O34	0.31×10^{-1}	0.94×10^{-1}	0.23×10^{-1}	-0.23×10^{-1}	0.92×10^{-4}
FAV@ B_3O_3 -C1						
81	N49-B7	0.80×10^{-2}	0.24×10^{-1}	0.52×10^{-2}	-0.44×10^{-2}	0.79×10^{-3}
95	H55-O34	0.17×10^{-1}	0.52×10^{-1}	0.13×10^{-1}	-0.13×10^{-1}	-0.26×10^{-3}
132	O56-B9	0.12×10^{-1}	0.33×10^{-1}	0.80×10^{-2}	-0.77×10^{-2}	0.22×10^{-3}
FAV@ B_3O_3 -C3						
24	H48-O34	0.42×10^0	-0.18×10^2	0.68×10^{-2}	-0.46×10^1	-0.46×10^1
65	H57-O39	0.25×10^{-1}	0.71×10^{-1}	0.18×10^{-1}	-0.19×10^{-1}	0.49×10^3
126	O56-O41	0.11×10^{-1}	0.35×10^{-1}	0.82×10^{-2}	-0.77×10^{-2}	0.52×10^3
FAV@ B_3O_3 -SW1						
66	O56-H1	0.54×10^{-2}	0.19×10^{-1}	0.38×10^{-2}	-0.29×10^{-2}	0.93×10^{-3}
109	N49-O40	0.79×10^{-2}	0.26×10^{-1}	0.59×10^{-2}	-0.53×10^{-2}	0.60×10^{-3}
119	F51-H5	0.36×10^{-2}	0.16×10^{-1}	0.31×10^{-2}	-0.20×10^{-2}	0.11×10^{-2}

The average values of ρ in favipiravir-adsorbed B_3O_3 complexes such as FAV@ B_3O_3 -C, FAV@ B_3O_3 -C1, FAV@ B_3O_3 -C3, and FAV@ B_3O_3 -SW1 range from 0.80×10^{-2} to 0.42×10^0 , respectively. The positive values of H in these complexes indicate the presence of non-covalent interactions in all reported complexes. However, the negative values of H in

some of the critical points of the complexes also depict the existence of hydrogen bonding, which is comparable to the NCI results (vide supra).

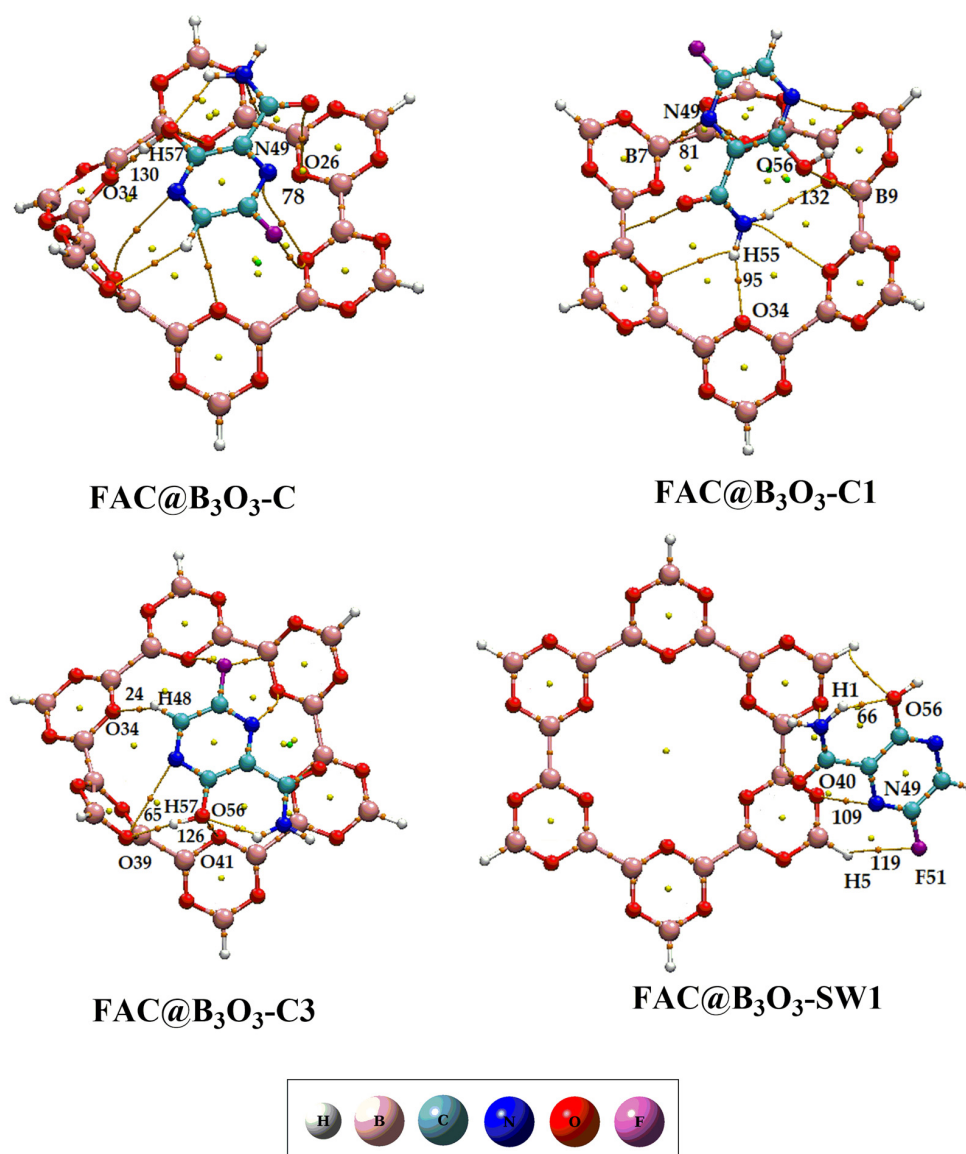


Figure 4. QTAIM analysis of favipiravir@B₃O₃ complexes (FAV@B₃O₃-C, FAV@B₃O₃-C1, FAV@B₃O₃-C3, FAV@B₃O₃-SW1).

2.4. Electronic Properties

The computation of frontier molecular orbitals is carried out to evaluate the electronic properties of drug and B₃O₃ nanoflake. According to the literature, the electronic behavior of a surface undergoes changes when they interact with any chemical species [50,51]. Table 3 and Figure 5 exhibit the energies of the HOMO and LUMO orbitals, as well as their corresponding isosurfaces. The energy gap between the HOMO and LUMO of pure B₃O₃ is determined to be 9.95 eV. However, upon complexation with the considered drug, the energy gap between HOMO and LUMO orbitals of FAV@B₃O₃-C, FAV@B₃O₃-C1, FAV@B₃O₃-C3 and FAV@B₃O₃-SW1 complexes is decreased. Specifically, the energy gap between the HOMO and LUMO orbitals for FAV@B₃O₃-C, FAV@B₃O₃-C1, FAV@B₃O₃-C3 and FAV@B₃O₃-SW1 complexes is 8.62, 8.67, 8.61 and 8.70 eV, respectively. The isosurface visualization of the HOMO and LUMO provides insights into the localization of the HOMO on the bonds in drug molecules in all of the doped complexes, while the LUMO is localized

on the atoms of the drug as well. The dipole moment is another crucial factor that defines the solubility and polarity of the system [52].

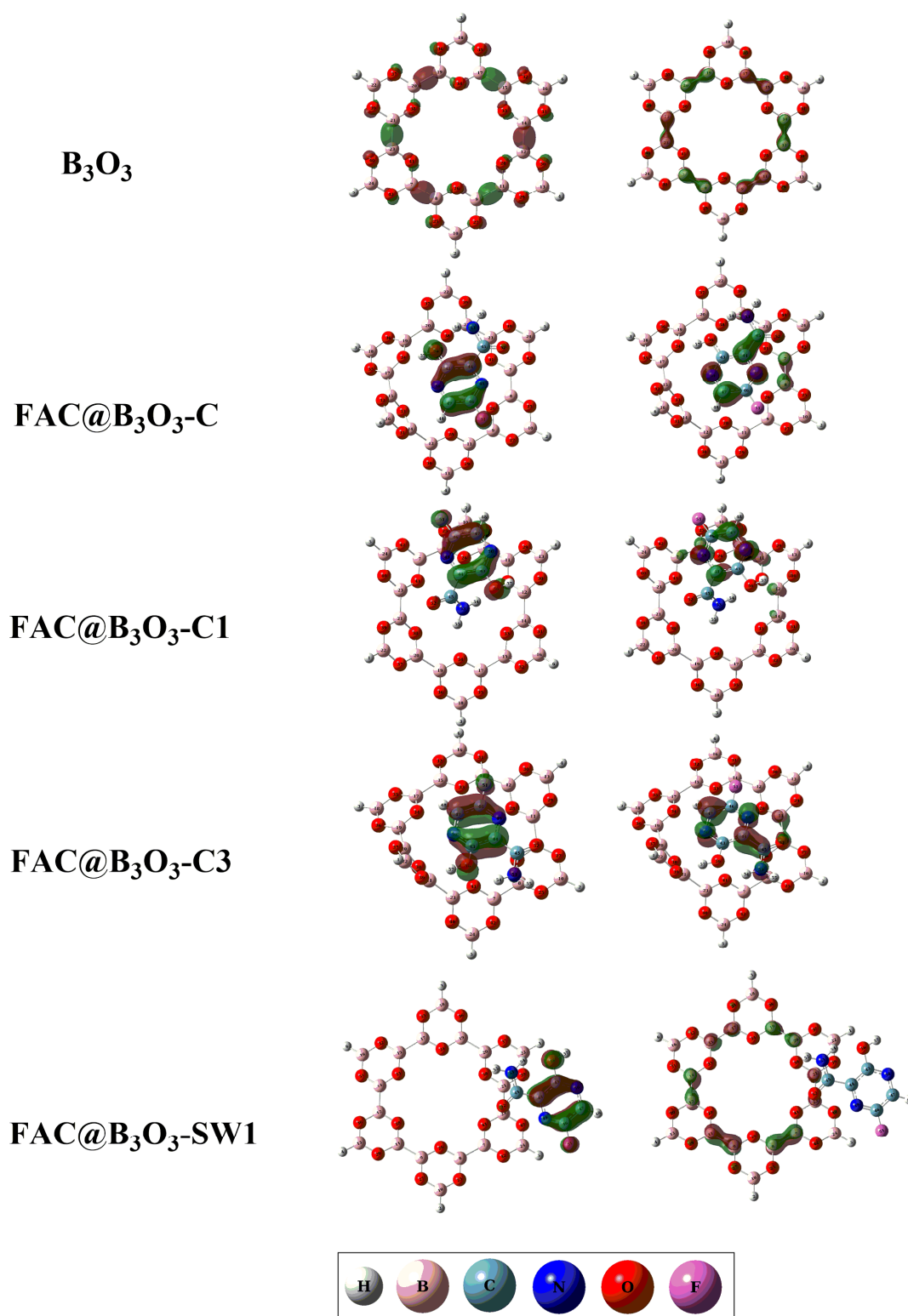


Figure 5. The HOMO and LUMO isosurface of the FAV@ B_3O_3 complexes (bare B_3O_3 , favipiravir, FAV@ B_3O_3-C , FAV@ B_3O_3-C1 , FAV@ B_3O_3-C3 and FAV@ B_3O_3-SW1).

Table 3. The electronic descriptors include the energy gap (E_{L-H}), softness (s), hardness (η), chemical potential (μ) and electrophilicity index (ω) in eV for the FAV@B₃O₃-C, FAV@B₃O₃-C1, FAV@B₃O₃-C3 and FAV@B₃O₃-SW1 complexes.

Complexes	E_{HOMO}	E_{LUMO}	E_{L-H}	s	η	μ	ω
B ₃ O ₃	−10.42	−0.46	9.96	0.10	4.98	−5.44	2.96
Favipiravir	−9.51	−0.72	8.79	0.11	4.40	−5.11	2.97
FAV@B ₃ O ₃ -C	−9.53	−0.89	8.64	0.12	4.32	−5.21	3.14
FAV@B ₃ O ₃ -C1	−9.54	−0.85	8.69	0.11	4.34	−5.20	3.11
FAV@B ₃ O ₃ -C3	−9.59	−0.97	8.62	0.12	4.31	−5.28	3.23
FAV@B ₃ O ₃ -SW1	−9.59	−0.88	8.71	0.11	4.36	−5.23	3.13

For the B₃O₃ nanoflakes, the dipole moment is measured to be 0.00 Debye, indicating their non-polar nature. However, the dipole moment in the FAV@B₃O₃-C, FAV@B₃O₃-C1, FAV@B₃O₃-C3 and FAV@B₃O₃-SW1 complexes is 5.96 D, 5.46 D, and 6.01 and 6.37 Debye, respectively. The dipole moment values of the reported FAV@B₃O₃ complexes demonstrate that the B₃O₃ nanoflakes acquire polarity upon interaction with the respective drug. This polarity arises from the Coulombic interactions between the nucleophilic cavities of B₃O₃ and the electrophilic hydrogen atoms of the drug in the doped complexes, especially in the FAV@B₃O₃-C1, FAV@B₃O₃-C3 and FAV@B₃O₃-C complexes. The dipole moments of FAV@B₃O₃-C1 and FAV@B₃O₃-C3 indicate that these complexes are reasonably soluble in an aqueous medium. On the other hand, FAV@B₃O₃-SW1 is relatively less soluble due to the absence of Coulombic interactions. Good solubility is typically a desirable property for a drug delivery system, which is evident in the FAV@B₃O₃-C1, FAV@B₃O₃-C3 and FAV@B₃O₃-C complexes.

The reactivity of favipiravir with the B₃O₃ quantum dots is evaluated using chemical reactive descriptors such as hardness (η), softness (s), chemical potential (μ), and electrophilicity index (ω) (see Table 3). The results indicate that the chemical potential (μ) of the respective drug-doped B₃O₃ complexes is higher than that of both the bare B₃O₃ nanosheets and the drug molecule. Furthermore, the high softness (s) values and low hardness (η) values follow the same trend as the chemical potential, indicating the stability of the doped complexes after complexation when compared to bare B₃O₃. Notably, the FAV@B₃O₃-C3 complex exhibits the highest softness (0.12 eV) value and the lowest hardness value (4.31 eV), indicating its lower reactivity and higher stability among all of the designed complexes. The FAV@B₃O₃-C3 complex also has the highest chemical potential (−5.28 eV) and electrophilicity index (3.23 eV) compared to the other bare and doped complexes. The higher chemical potential indicates greater charge transfer in this FAV@B₃O₃-C3 complex and the high electrophilicity index justifies the higher stabilization energy of the doped complex. The FAV@B₃O₃-SW1 complex exhibits the lowest softness (0.11 eV) value and the highest hardness value (4.36 eV), indicating lower stability and high reactivity among all designed complexes. On the other hand, the FAV@B₃O₃-C1 complex has the lowest chemical potential (−5.26 eV) and electrophilicity index (3.11 eV). These results indicate the lower charge transfer and lower stabilization energy of the FAV@B₃O₃-C1 complex. The high electrophilicity, low hardness, high softness, and high chemical potential values collectively suggest that B₃O₃ can serve as an effective drug delivery system for favipiravir.

2.5. UV-VIS Analysis

The UV-Vis analysis plays a crucial role in comprehending the behavior of the sensor as an optical sensor. As per the existing literature, a rise in the interaction energy between two chemical species is projected to cause a change in wavelength for an optical sensor [11]. Figure 6 and Table 3 present the UV-Vis spectra and corresponding values for both the bare and complexed B₃O₃. The absorbance of bare B₃O₃ was observed at 221 nm. However, upon complexation with favipiravir, this absorbance shifts towards higher wavelengths, as

observed in our previous report [38]. The λ_{\max} of B_3O_3 experiences a shift to 273 nm, 266 nm, 274 nm and 269 nm for FAV@ B_3O_3 -C, FAV@ B_3O_3 -C1, FAV@ B_3O_3 -C3 and FAV@ B_3O_3 -SW1 complexes, respectively (Figure 6). This red shift is observed for all of the doped complexes. The UV-Vis analysis justifies electronic excitation in doped complexes due to the strong interaction between the drug and the B_3O_3 surface. These findings strongly indicate the effectiveness of B_3O_3 for optical sensing applications involving the antiviral drug favipiravir.

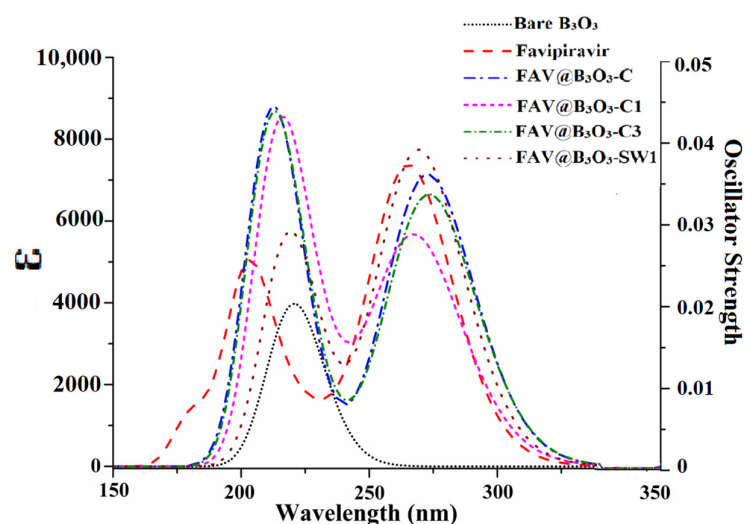


Figure 6. UV-Vis analysis of the FAV@ B_3O_3 complexes (bare B_3O_3 , favipiravir, FAV@ B_3O_3 -C, FAV@ B_3O_3 -C1, FAV@ B_3O_3 -C3 and FAV@ B_3O_3 -SW1).

Internal descriptors including the oscillating strength and excitation energies are calculated to understand the reason for the change in wavelength. The wavelength is directly proportional to the oscillating strength and inversely proportional to the excitation energy. The FAV@ B_3O_3 -C has a maximum wavelength of 273 nm and an oscillating strength of 0.170. The FAV@ B_3O_3 -C1 has a maximum wavelength of 266 nm and an oscillating strength of 0.119. The trend of increasing f_o is comparable to the increase in wavelength. The excitation energy also decreases for doped complexes compared to bare B_3O_3 (5.62 eV). The excitation energy ranges from 4.53 to 4.67 eV. The trend of increasing wavelength is similar to the increase in excitation energy. The lowest excitation energy (4.53 eV) is seen for FAV@ B_3O_3 -C3, which has a maximum wavelength of 274 nm. The lowest excitation energy is 4.66 eV for FAV@ B_3O_3 -C3, which has a maximum wavelength of 266 nm. The excitation energy is the dominating factor responsible for causing changes in the wavelength of the doped complexes (Table 4).

Table 4. The maximum wavelength (λ_{\max} in nm), oscillating strength (f_o) and excitation energy (in eV) of bare B_3O_3 , favipiravir, FAV@ B_3O_3 -C, FAV@ B_3O_3 -C1, FAV@ B_3O_3 -C3 and FAV@ B_3O_3 -SW1 complexes.

Complex	Wavelength (nm)	Oscillating Strength (f_o)	Excitation energy (eV)
B_3O_3	221	0.098	5.62
Favipiravir	265	0.179	4.67
FAV@ B_3O_3 -C	273	0.170	4.54
FAV@ B_3O_3 -C1	266	0.119	4.66
FAV@ B_3O_3 -C3	274	0.154	4.53
FAV@ B_3O_3 -SW1	269	0.182	4.60

3. Materials and Methods

Computational Methodology

DFT simulations were conducted using Gaussian 09 [53], while the GaussView 5.0 [54] software package was used for visualization. Geometric analysis utilized the ω B97XD functional in conjunction with the 6-31+G(d,p) basis set. The ω B97XD functional is a hybrid and long-range separated functional with additional dispersion correction, and is popular due to its treatment of non-covalent interactions [55–57]. This correction factor accounts for weak London dispersion forces and ensures the production of accurate optimization results [58,59]. The interaction (E_{int}) and counterpoise-corrected (E_{cp}) energies were calculated by using Equations (1) and (2):

$$E_{\text{int}} = E_{\text{FAV-B}_3\text{O}_3} - [E_{\text{FAV}} + E_{\text{B}_3\text{O}_3}] \quad (1)$$

$$E_{\text{cp}} = E_{\text{FAV-B}_3\text{O}_3} - [E_{\text{FAV}} + E_{\text{B}_3\text{O}_3}] + \text{BSSE} \quad (2)$$

where $E_{\text{FAV@B}_3\text{O}_3}$, E_{FAV} , and $E_{\text{B}_3\text{O}_3}$ represent the energies of the FAV@B₃O₃ complexes, favipiravir (FAV), and the B₃O₃ surface, respectively. BSSE refers to the basis set superposition error caused by overlapping basis sets, and it was corrected by using the counterpoise method specified in Gaussian 09 [58]. The interaction energies indicate the non-covalent physisorption of favipiravir onto the surface of the B₃O₃ nanoflakes. To evaluate the non-covalent interactive and repulsive forces, non-covalent interaction index (NCI) and quantum theory of atoms in molecules (QTAIM) analyses were performed using Multiwfn 3.8 software [60].

Electronic properties were investigated at the ω B97XD/6-31+G(d,p) level of theory. ω B97XD is a highly reliable functional widely used for investigating the electronic properties of various systems, providing energy gaps comparable to experimental data [61–63]. NBO charge transfer calculations were conducted to determine the extent of charge transfer between the interacting moieties (drug and surface). Additionally, electronic descriptors such as the chemical hardness, softness, chemical potential, and electrophilicity index were computed to analyze the reactivity of the systems:

$$\eta = E_{\text{LUMO}} - E_{\text{HOMO}}/2 \quad (3)$$

$$S = 1/2\eta \quad (4)$$

$$\mu = E_{\text{HOMO}} + E_{\text{LUMO}}/2 \quad (5)$$

$$\omega = \mu^2/2\eta \quad (6)$$

4. Conclusions

B₃O₃ nanoflakes are analyzed as drug carriers for the antiviral drug favipiravir using DFT simulations. The strong interactions between both species (boron oxide and favipiravir) depict their thermodynamic stability. Four orientations are investigated for the interaction between favipiravir and the B₃O₃. The E_{int} of the most stable orientation is -26.98 kcal/mol, whereas the counterpoise-corrected energy is -22.59 kcal/mol. The electronic properties are investigated through frontier molecular orbital analysis, dipole moments and chemical reactivity descriptors. These parameters indicate the significant activity of B₃O₃ nanoflakes for favipiravir. NBO charge transfer illustrates the charge transfer between the interacting species. Noncovalent interaction index (NCI) and quantum theory of atoms in molecules (QTAIM) analyses are performed to gain insights about the behavior and the types of interactions that occur between B₃O₃ quantum dots and favipiravir. The results indicate the presence of hydrogen bonding between the hydrogen of the favipiravir and the oxygen of the B₃O₃ quantum dots in the most stable complex (FAV@B₃O₃-C1). UV-Vis analysis confirmed the electronic excitation. All of the complexes showed red shift compared to bare B₃O₃ quantum dots and favipiravir. Our work provides a suitable drug carrier system

for the antiviral drug favipiravir, which can be considered by the experimentalist for better drug delivery systems.

Author Contributions: Conceptualization, T.M. and K.E.I.; Methodology, M.N.Z. and N.K.; Validation, T.M. and H.S.; Formal analysis, N.K., M.N.Z. and H.S.; Investigation, M.N.Z. and N.K.; Resources, T.M. and M.K.G.; Data curation, M.N.Z., N.K. and H.S.; Writing—original draft, M.N.Z. and N.K.; Writing—review & editing, T.M., K.E.I. and M.K.G.; Supervision, T.M.; Project administration, K.E.I. and M.K.G.; Funding acquisition, K.E.I. and M.K.G. All authors have read and agreed to the published version of the manuscript.

Funding: Researchers Supporting Project (RSP2023R393), King Saud University, Riyadh, Saudi Arabia.

Institutional Review Board Statement: Not applicable.

Informed Consent Statement: Not applicable.

Data Availability Statement: Data will be made available to the corresponding author upon request.

Acknowledgments: The authors acknowledge Researchers Supporting Project (RSP2023R393), King Saud University, Riyadh, Saudi Arabia, Higher Education Commission of Pakistan and University of Bahrain for their financial support of current research.

Conflicts of Interest: The authors declare no conflict of interest.

References

1. Agrawal, U.; Raju, R.; Udawadia, Z.F. Favipiravir: A New and Emerging Antiviral Option in COVID-19. *Med. J. Armed Forces India* **2020**, *76*, 370–376. [[CrossRef](#)]
2. Furuta, Y.; Gowen, B.B.; Takahashi, K.; Shiraki, K.; Smees, D.F.; Barnard, D.L. Favipiravir (T-705), a Novel Viral RNA Polymerase Inhibitor. *Antivir. Res.* **2013**, *100*, 446–454. [[CrossRef](#)]
3. Pandey, A.; Yadav, S. Essentials of COVID-19 and Treatment Approaches. In *Data Science for COVID-19*; Elsevier: Amsterdam, The Netherlands, 2022; pp. 397–422.
4. Sissoko, D.; Laouenan, C.; Folkesson, E.; M'Lebing, A.-B.; Beavogui, A.-H.; Baize, S.; Camara, A.-M.; Maes, P.; Shepherd, S.; Danel, C.; et al. Experimental Treatment with Favipiravir for Ebola Virus Disease (the JIKI Trial): A Historically Controlled, Single-Arm Proof-of-Concept Trial in Guinea. *PLoS Med.* **2016**, *13*, e1001967. [[CrossRef](#)]
5. Chen, P.; Nirula, A.; Heller, B.; Gottlieb, R.L.; Boscia, J.; Morris, J.; Huhn, G.; Cardona, J.; Mocherla, B.; Stosor, V.; et al. SARS-CoV-2 Neutralizing Antibody LY-CoV555 in Outpatients with COVID-19. *N. Engl. J. Med.* **2021**, *384*, 229–237. [[CrossRef](#)] [[PubMed](#)]
6. Aggarwal, K.; Agarwal, A.; Jaiswal, N.; Dahiya, N.; Ahuja, A.; Mahajan, S.; Tong, L.; Duggal, M.; Singh, M.; Agrawal, R.; et al. Ocular Surface Manifestations of Coronavirus Disease 2019 (COVID-19): A Systematic Review and Meta-Analysis. *PLoS ONE* **2020**, *15*, e0241661. [[CrossRef](#)] [[PubMed](#)]
7. Torchilin, V.P. Multifunctional, Stimuli-Sensitive Nanoparticulate Systems for Drug Delivery. *Nat. Rev. Drug Discov.* **2014**, *13*, 813–827. [[CrossRef](#)] [[PubMed](#)]
8. Bryan, C.J.; Mintz, J.; Clemans, T.A.; Leeson, B.; Burch, T.S.; Williams, S.R.; Maney, E.; Rudd, M.D. Effect of Crisis Response Planning vs. Contracts for Safety on Suicide Risk in U.S. Army Soldiers: A Randomized Clinical Trial. *J. Affect. Disord.* **2017**, *212*, 64–72. [[CrossRef](#)] [[PubMed](#)]
9. Xie, X.; Wang, L.; Zeng, S. Inter-Organizational Knowledge Acquisition and Firms' Radical Innovation: A Moderated Mediation Analysis. *J. Bus. Res.* **2018**, *90*, 295–306. [[CrossRef](#)]
10. Mariadoss, A.V.A.; Saravanakumar, K.; Sathiyaseelan, A.; Venkatachalam, K.; Wang, M.-H. Folic Acid Functionalized Starch Encapsulated Green Synthesized Copper Oxide Nanoparticles for Targeted Drug Delivery in Breast Cancer Therapy. *Int. J. Biol. Macromol.* **2020**, *164*, 2073–2084. [[CrossRef](#)]
11. Nagarajan, V.; Chandiramouli, R. NiO Nanocone as a CO Sensor: DFT Investigation. *Struct. Chem.* **2014**, *25*, 1765–1771. [[CrossRef](#)]
12. Chandiramouli, R.; Nagarajan, V. Borospherene Nanostructure as CO and NO Sensor—A First-Principles Study. *Vacuum* **2017**, *142*, 13–20. [[CrossRef](#)]
13. Chandiramouli, R.; Jeyaprakash, B.G. Review of CdO Thin Films. *Solid State Sci.* **2013**, *16*, 102–110. [[CrossRef](#)]
14. Bhuvaneshwari, R.; Nagarajan, V.; Chandiramouli, R. Arsenene Nanoribbons for Sensing NH₃ and PH₃ Gas Molecules—A First-Principles Perspective. *Appl. Surf. Sci.* **2019**, *469*, 173–180. [[CrossRef](#)]
15. Padesh, R.; Sobhani-Nasab, A.; Rahimi-Nasrabadi, M.; Mirmotahari, M.; Ehrlich, H.; Rad, A.S.; Peyravi, M. Is It Possible to Use X₁₂Y₁₂ (X = Al, B, and Y = N, P) Nanocages for Drug-Delivery Systems? A DFT Study on the Adsorption Property of 4-Aminopyridine Drug. *Appl. Phys. A* **2018**, *124*, 582. [[CrossRef](#)]
16. Rahimi, R.; Solimannejad, M. B₃O₃ Monolayer with Dual Application in Sensing of COVID-19 Biomarkers and Drug Delivery for Treatment Purposes: A Periodic DFT Study. *J. Mol. Liq.* **2022**, *354*, 118855. [[CrossRef](#)]
17. Vatanparast, M.; Shariatinia, Z. Hexagonal Boron Nitride Nanosheet as Novel Drug Delivery System for Anticancer Drugs: Insights from DFT Calculations and Molecular Dynamics Simulations. *J. Mol. Graph. Model.* **2019**, *89*, 50–59. [[CrossRef](#)] [[PubMed](#)]

18. Sakr, A.K.; Al-Hamarneh, I.F.; Gomaa, H.; Abdel Aal, M.M.; Hanfi, M.Y.; Sayyed, M.I.; Khandaler, M.U.; Cheira, M.F. Removal of Uranium from Nuclear Effluent Using Regenerated Bleaching Earth Steeped in B-naphthol. *Radiat. Phys. Chem.* **2022**, *200*, 110204. [[CrossRef](#)]
19. Bhuvaneshwari, R.; Princy Maria, J.; Nagarajan, V.; Chandiramouli, R. Graphdiyne Nanosheets as a Sensing Medium for Formaldehyde and Formic Acid—A First-Principles Outlook. *Comput. Theor. Chem.* **2020**, *1176*, 112751. [[CrossRef](#)]
20. Mujtaba Munir, M.A.; Yousaf, B.; Ali, M.U.; Dan, C.; Abbas, Q.; Arif, M.; Yang, X. In Situ Synthesis of Micro-Plastics Embedded Sewage-Sludge Co-Pyrolyzed Biochar: Implications for the Remediation of Cr and Pb Availability and Enzymatic Activities from the Contaminated Soil. *J. Clean. Prod.* **2021**, *302*, 127005. [[CrossRef](#)]
21. Perveen, S.; Akram, M.; Nasar, A.; Arshad-Ayaz, A.; Naseem, A. Vaccination-hesitancy and Vaccination-inequality as Challenges in Pakistan's COVID-19 Response. *J. Community Psychol.* **2022**, *50*, 666–683. [[CrossRef](#)]
22. Zeenat; Elahi, A.; Bukhari, D.A.; Shamim, S.; Rehman, A. Plastics Degradation by Microbes: A Sustainable Approach. *J. King Saud Univ.—Sci.* **2021**, *33*, 101538. [[CrossRef](#)]
23. Srimathi, U.; Nagarajan, V.; Chandiramouli, R. Investigation on Graphdiyne Nanosheet in Adsorption of Sorafenib and Regorafenib Drugs: A DFT Approach. *J. Mol. Liq.* **2019**, *277*, 776–785. [[CrossRef](#)]
24. Yang, F.; Wang, X.; Li, M.; Liu, X.; Zhao, X.; Zhang, D.; Zhang, Y.; Yang, J.; Li, Y. Templated Synthesis of Single-Walled Carbon Nanotubes with Specific Structure. *Acc. Chem. Res.* **2016**, *49*, 606–615. [[CrossRef](#)] [[PubMed](#)]
25. Niu, Y.; Shen, B.; Cui, Y.; Chen, Y.; Wang, J.; Wang, L.; Kang, Y.; Zhao, X.; Si, W.; Li, W.; et al. Generation of Gene-Modified Cynomolgus Monkey via Cas9/RNA-Mediated Gene Targeting in One-Cell Embryos. *Cell* **2014**, *156*, 836–843. [[CrossRef](#)]
26. Schwierz, F. Graphene Transistors. *Nat. Nanotechnol.* **2010**, *5*, 487–496. [[CrossRef](#)] [[PubMed](#)]
27. Singh Raman, R.K.; Tiwari, A. Graphene: The Thinnest Known Coating for Corrosion Protection. *JOM* **2014**, *66*, 637–642. [[CrossRef](#)]
28. Barzan Talab, M.; Hasan Muttashar, H.; Faraj, J.; Abdullaha, S.A.H.; Hachim, S.K.; Adel, M.; Kadhim, M.M.; Mahdi Rheima, A. Inspection the Potential of B₃O₃ Monolayer as a Carrier for Flutamide Anticancer Delivery System. *Comput. Theor. Chem.* **2022**, *1217*, 113886. [[CrossRef](#)]
29. Li, H.-Y.; Zhao, S.-N.; Zang, S.-Q.; Li, J. Functional Metal–Organic Frameworks as Effective Sensors of Gases and Volatile Compounds. *Chem. Soc. Rev.* **2020**, *49*, 6364–6401. [[CrossRef](#)]
30. Li, M.; Cushing, S.K.; Wu, N. Plasmon-Enhanced Optical Sensors: A Review. *Analyst* **2015**, *140*, 386–406. [[CrossRef](#)]
31. Florensa, M.; Llenas, M.; Medina-Gutiérrez, E.; Sandoval, S.; Tobias-Rossell, G. Key Parameters for the Rational Design, Synthesis, and Functionalization of Biocompatible Mesoporous Silica Nanoparticles. *Pharmaceutics* **2022**, *14*, 2703. [[CrossRef](#)]
32. Vatanparast, M.; Shariatnia, Z. Revealing the Role of Different Nitrogen Functionalities in the Drug Delivery Performance of Graphene Quantum Dots: A Combined Density Functional Theory and Molecular Dynamics Approach. *J. Mater. Chem. B* **2019**, *7*, 6156–6171. [[CrossRef](#)] [[PubMed](#)]
33. Cheng, M.; Jin, C.; Jin, W.; Hou, X. Target-Oriented Synthesis of Borate Derivatives Featuring Isolated [B₃O₃] Six-Membered Rings as Structural Features. *Inorg. Chem.* **2023**, *62*, 9209–9216. [[CrossRef](#)] [[PubMed](#)]
34. Wei, S.; Li, A.; Liu, J.-C.; Li, Z.; Chen, W.; Gong, Y.; Zhang, Q.; Cheong, W.-C.; Wang, Y.; Zheng, L.; et al. Direct Observation of Noble Metal Nanoparticles Transforming to Thermally Stable Single Atoms. *Nat. Nanotechnol.* **2018**, *13*, 856–861. [[CrossRef](#)] [[PubMed](#)]
35. Stredansky, M.; Sala, A.; Fontanot, T.; Costantini, R.; Africh, C.; Comelli, G.; Floreano, L.; Morgante, A.; Cossaro, A. On-Surface Synthesis of a 2D Boroxine Framework: A Route to a Novel 2D Material? *Chem. Commun.* **2018**, *54*, 3971–3973. [[CrossRef](#)] [[PubMed](#)]
36. Lin, K.; Xing, J.; Quan, L.N.; de Arquer, F.P.G.; Gong, X.; Lu, J.; Xie, L.; Zhao, W.; Zhang, D.; Yan, C.; et al. Perovskite Light-Emitting Diodes with External Quantum Efficiency Exceeding 20 per Cent. *Nature* **2018**, *562*, 245–248. [[CrossRef](#)] [[PubMed](#)]
37. Lin, S.; Gu, J.; Zhang, H.; Wang, Y.; Chen, Z. Porous Hexagonal Boron Oxide Monolayer with Robust Wide Band Gap: A Computational Study. *FlatChem* **2018**, *9*, 27–32. [[CrossRef](#)]
38. Nauman Zahid, M.; Asif, M.; Sajid, H.; Kosar, N.; Akbar Shahid, M.; Allangawi, A.; Ayub, K.; Azeem, M.; Mahmood, T. Therapeutic Efficiency of B₃O₃ Quantum Dot as a Targeted Drug Delivery System toward Foscarnet Anti-HIV Drug. *Comput. Theor. Chem.* **2023**, *1224*, 114107. [[CrossRef](#)]
39. Rahimi, R.; Solimannejad, M.; Ehsanfar, Z. First-Principles Studies on Two-Dimensional B₃O₃ Adsorbent as a Potential Drug Delivery Platform for TEPA Anticancer Drug. *J. Mol. Model.* **2021**, *27*, 347. [[CrossRef](#)]
40. Carrera Espinoza, M.J.; Lin, K.-S.; Weng, M.-T.; Kunene, S.C.; Lin, Y.-S.; Liu, S.-Y. Magnetic Boron Nitride Nanosheets-Based on PH-Responsive Smart Nanocarriers for the Delivery of Doxorubicin for Liver Cancer Treatment. *Colloids Surf. B Biointerfaces* **2023**, *222*, 113129. [[CrossRef](#)]
41. Saha, S.K.; Murmu, M.; Murmu, N.C.; Obot, I.B.; Banerjee, P. Molecular Level Insights for the Corrosion Inhibition Effectiveness of Three Amine Derivatives on the Carbon Steel Surface in the Adverse Medium: A Combined Density Functional Theory and Molecular Dynamics Simulation Study. *Surf. Interfaces* **2018**, *10*, 65–73. [[CrossRef](#)]
42. Trabelsi, S.; Tlili, M.; Abdelmoulaoui, H.; Bouazizi, S.; Nasr, S.; González, M.A.; Bellissent-Funel, M.-C.; Darpentigny, J. Intermolecular Interactions in an Equimolar Methanol-Water Mixture: Neutron Scattering, DFT, NBO, AIM, and MD Investigations. *J. Mol. Liq.* **2022**, *349*, 118131. [[CrossRef](#)]

43. Fariás-Rico, J.A.; Ruud Selin, F.; Myronidi, I.; Frühauf, M.; von Heijne, G. Effects of Protein Size, Thermodynamic Stability, and Net Charge on Cotranslational Folding on the Ribosome. *Proc. Natl. Acad. Sci. USA* **2018**, *115*, E9280–E9287. [[CrossRef](#)] [[PubMed](#)]
44. Zhao, R.; Wang, T.; An, Y.; Dai, X.; Xia, C. VS₂ Nanosheet as a Promising Candidate of Recycle and Reuse NO₂ Gas Sensor and Capturer: A DFT Study. *J. Phys. Condens. Matter* **2021**, *33*, 165501. [[CrossRef](#)] [[PubMed](#)]
45. Berendsen, H.J.C.; Postma, J.P.M.; van Gunsteren, W.F.; DiNola, A.; Haak, J.R. Molecular Dynamics with Coupling to an External Bath. *J. Chem. Phys.* **1984**, *81*, 3684–3690. [[CrossRef](#)]
46. Ghalla, H.; Issaoui, N.; Bardak, F.; Atac, A. Intermolecular Interactions and Molecular Docking Investigations on 4-Methoxybenzaldehyde. *Comput. Mater. Sci.* **2018**, *149*, 291–300. [[CrossRef](#)]
47. Issaoui, N.; Abdessalem, K.; Ghalla, H.; Yaghmour, S.J.; Calvo, F.; Oujia, B. Theoretical Investigation of the Relative Stability of Na + He n (n = 2–24) Clusters: Many-Body versus Delocalization Effects. *J. Chem. Phys.* **2014**, *141*, 174316. [[CrossRef](#)]
48. Cremer, D.; Kraka, E. Chemical Bonds without Bonding Electron Density? Does the Difference Electron-Density Analysis Suffice for a Description of the Chemical Bond? *Angew. Chem. Int. Ed. Engl.* **1984**, *23*, 627–628. [[CrossRef](#)]
49. Jenkins, S.; Morrison, I. The Chemical Character of the Intermolecular Bonds of Seven Phases of Ice as Revealed by Ab Initio Calculation of Electron Densities. *Chem. Phys. Lett.* **2000**, *317*, 97–102. [[CrossRef](#)]
50. Khan, S.; Yar, M.; Kosar, N.; Ayub, K.; Arshad, M.; Zahid, M.N.; Mahmood, T. First-Principles Study for Exploring the Adsorption Behavior of G-Series Nerve Agents on Graphdyne Surface. *Comput. Theor. Chem.* **2020**, *1191*, 113043. [[CrossRef](#)]
51. Asif, M.; Sajid, H.; Kosar, N.; Mahmood, T. Effect of Fluorination on the Adsorption Properties of Aromatic Heterocycles toward Methyl Halides: A Quantum Chemical Study. *Comput. Theor. Chem.* **2021**, *1204*, 113394. [[CrossRef](#)]
52. Perveen, M.; Nazir, S.; Arshad, A.W.; Khan, M.I.; Shamim, M.; Ayub, K.; Khan, M.A.; Iqbal, J. Therapeutic Potential of Graphitic Carbon Nitride as a Drug Delivery System for Cisplatin (Anticancer Drug): A DFT Approach. *Biophys. Chem.* **2020**, *267*, 106461. [[CrossRef](#)]
53. Frisch, M.J.; Trucks, G.W.; Schlegel, J.; Scuseria, G.E.; Robb, M.A.; Cheeseman, J.R.; Schlegel, H.B.; Scalmani, G.; Barone, V.; Mennucci, B. *Gaussian 09, Rev. C.01*; Gaussian, Inc.: Wallingford, CT, USA, 2010.
54. Dennington, R.; Keith, T.; Millam, J. *GaussView 5.0*; Semichem Inc.: Shawnee Mission, KS, USA, 2009.
55. Su, H.; Wang, H.; Wang, H.; Lu, Y.; Zhu, Z. Description of Noncovalent Interactions Involving π -system with High Precision: An Assessment of RPA, MP2, and DFT-D Methods. *J. Comput. Chem.* **2019**, *40*, 1643–1651. [[CrossRef](#)] [[PubMed](#)]
56. Bandyopadhyay, P.; Karmakar, A.; Deb, J.; Sarkar, U.; Seikh, M.M. Non-Covalent Interactions between Epinephrine and Nitroaromatic Compounds: A DFT Study. *Spectrochim. Acta Part A Mol. Biomol. Spectrosc.* **2020**, *228*, 117827. [[CrossRef](#)] [[PubMed](#)]
57. Jia, Z.; Pang, H.; Li, H.; Wang, X. A Density Functional Theory Study on Complexation Processes and Intermolecular Interactions of Triptycene-Derived Oxacalixarenes. *Theor. Chem. Acc.* **2019**, *138*, 113. [[CrossRef](#)]
58. Turi, L.; Dannenberg, J.J. Correcting for Basis Set Superposition Error in Aggregates Containing More than Two Molecules: Ambiguities in the Calculation of the Counterpoise Correction. *J. Phys. Chem.* **1993**, *97*, 2488–2490. [[CrossRef](#)]
59. Hasan, P. Antimonachismus v České Osvícenské Společnosti. *Cornova* **2013**, *3*, 83–100. [[CrossRef](#)]
60. Lu, T.; Chen, F. Multiwfn: A Multifunctional Wavefunction Analyzer. *J. Comput. Chem.* **2012**, *33*, 580–592. [[CrossRef](#)] [[PubMed](#)]
61. De Castro, E.A.S.; de Oliveira, D.A.B.; Farias, S.A.S.; Gargano, R.; Martins, J.B.L. Structure and Electronic Properties of Azadirachtin. *J. Mol. Model.* **2014**, *20*, 2084. [[CrossRef](#)] [[PubMed](#)]
62. Cooper, J.; Zhang, J.; Grant, C. Ab Initio Calculation of Ionization Potential and Electron Affinity of Six Common Explosive Compounds. *Rep. Theor. Chem.* **2012**, *1*, 11–19. [[CrossRef](#)]
63. Alp, M.; Yurdakul, S. Experimental and Theoretical Vibrational Spectroscopic, Quantum Chemical Analysis, and Electronic Properties Investigations of Novel Ruthenium Complexes (RuLCl₂·2H₂O; L: 4,4'-Dimethoxy-2,2'-Bipyridine, 4,4'-Dimethyl-2,2'-Bipyridine). *Polyhedron* **2023**, *234*, 116322. [[CrossRef](#)]

Disclaimer/Publisher's Note: The statements, opinions and data contained in all publications are solely those of the individual author(s) and contributor(s) and not of MDPI and/or the editor(s). MDPI and/or the editor(s) disclaim responsibility for any injury to people or property resulting from any ideas, methods, instructions or products referred to in the content.